

Article

# Modelling of XCO<sub>2</sub> Surfaces Based on Flight Tests of TanSat Instruments

Li Li Zhang<sup>1</sup>, Tian Xiang Yue<sup>1,\*</sup>, John P. Wilson<sup>1,2</sup>, Ding Yi Wang<sup>3</sup>, Na Zhao<sup>1</sup>, Yu Liu<sup>1</sup>, Dong Dong Liu<sup>3</sup>, Zheng Ping Du<sup>1</sup>, Yi Fu Wang<sup>1</sup>, Chao Lin<sup>4</sup>, Yu Quan Zheng<sup>4</sup> and Jian Hong Guo<sup>1</sup>

- <sup>1</sup> State Key Laboratory of Resources and Environment Information System, Institute of Geographical Sciences and Natural Resources Research, Chinese Academy of Sciences, Beijing 100101, China; zhangll@reis.ac.cn (L.L.Z.); jpwilson@dornsife.usc.edu (J.P.W.); zhaon@reis.ac.cn (N.Z.); liuyu.15b@igsrr.ac.cn (Y.L.); duzp@reis.ac.cn (Z.P.D.); wangyf@reis.ac.cn (Y.F.W.); gjh@irsa.ac.cn (J.H.G.)
  - <sup>2</sup> Spatial Sciences Institute, Dana and David Dornsife College of Letters, Arts, and Sciences, University of Southern California, Los Angeles, CA 90089-0374, USA
  - <sup>3</sup> Ministry of Education Key Laboratory for Nonequilibrium Synthesis and Modulation of Condensed Matter, School of Science, Xi'an Jiaotong University, Xi'an 710049, China; dingyiwang@hotmail.com (D.Y.W.); liudongdongzhijia@163.com (D.D.L.)
  - <sup>4</sup> Changchun Institute of Optics, Fine Mechanics and Physics, Chinese Academy of Sciences, Changchun 130033, China; linchaoluck@163.com (C.L.); zhengyq@sklao.ac.cn (Y.Q.Z.)
- \* Correspondence: yue@reis.ac.cn; Tel.: +86-10-6488-9041

Academic Editor: Assefa M. Melesse

Received: 16 August 2016; Accepted: 26 October 2016; Published: 1 November 2016

**Abstract:** The TanSat carbon satellite is to be launched at the end of 2016. In order to verify the performance of its instruments, a flight test of TanSat instruments was conducted in Jilin Province in September, 2015. The flight test area covered a total area of about 11,000 km<sup>2</sup> and the underlying surface cover included several lakes, forest land, grassland, wetland, farmland, a thermal power plant and numerous cities and villages. We modeled the column-average dry-air mole fraction of atmospheric carbon dioxide (XCO<sub>2</sub>) surface based on flight test data which measured the near- and short-wave infrared (NIR) reflected solar radiation in the absorption bands at around 760 and 1610 nm. However, it is difficult to directly analyze the spatial distribution of XCO<sub>2</sub> in the flight area using the limited flight test data and the approximate surface of XCO<sub>2</sub>, which was obtained by regression modeling, which is not very accurate either. We therefore used the high accuracy surface modeling (HASM) platform to fill the gaps where there is no information on XCO<sub>2</sub> in the flight test area, which takes the approximate surface of XCO<sub>2</sub> as its driving field and the XCO<sub>2</sub> observations retrieved from the flight test as its optimum control constraints. High accuracy surfaces of XCO<sub>2</sub> were constructed with HASM based on the flight's observations. The results showed that the mean XCO<sub>2</sub> in the flight test area is about 400 ppm and that XCO<sub>2</sub> over urban areas is much higher than in other places. Compared with OCO-2's XCO<sub>2</sub>, the mean difference is 0.7 ppm and the standard deviation is 0.95 ppm. Therefore, the modelling of the XCO<sub>2</sub> surface based on the flight test of the TanSat instruments fell within an expected and acceptable range.

**Keywords:** TanSat; flight test; XCO<sub>2</sub> retrieval; HASM; XCO<sub>2</sub> simulation

## 1. Introduction

Atmospheric carbon dioxide (CO<sub>2</sub>) is the dominant anthropogenic greenhouse gas, and a crucial factor in global climate change [1]. However, our current knowledge about the temporal and spatial variability of atmospheric CO<sub>2</sub> is still insufficient, which leads to large uncertainties in our estimates of carbon sources and sinks [2–4]. Ground-based observations, for example, are accurate but too spatially

sparse to sufficiently infer CO<sub>2</sub> sources and sinks [3,5–9]. Space-based measurements, on the other hand, have the potential to yield global estimates of the distribution of the atmospheric CO<sub>2</sub> vertical column (in molecules/cm<sup>2</sup>) or the CO<sub>2</sub> dry air column-averaged mole fraction (in ppm), especially in areas not covered by ground-based observations [5,10].

Near and short-wave infrared (NIR) measurements have sufficiently high precision and sensitivity to the planetary boundary layer, where the largest signals of sources and sinks occur [2,3,6,7,11–16]. The first NIR carbon satellite instrument, SCIAMACHY, onboard ENVISAT that was launched in 2002 and lost in 2012, measured reflected solar radiation in the NIR spectral bands [4,9]. Presently, there are only two NIR carbon satellite instruments orbiting the Earth, which enable the retrieval of XCO<sub>2</sub> with significant sensitivity in the boundary layer (i.e., near the Earth’s surface). The two instruments are TANSO, onboard GOSAT launched in 2009 and OCO-2 launched in 2014 [12–14]. China’s first satellite to monitor atmospheric XCO<sub>2</sub>, TanSat, will be launched at the end of 2016. A flight test was conducted in September, 2015 to evaluate the performance and stability of TanSat’s instruments for acquiring high resolution absorption spectra, and to reduce the risk of TanSat operating problems after launch. Simultaneous ground-based measurements of geophysical parameters were also collected and can be used to evaluate the accuracy of the retrieved atmospheric XCO<sub>2</sub> estimates.

The remainder of this article is structured as follows: Section 2 introduces the flight area and data used in this article. Section 3 introduces the methods used in this study, including the deployment of a full physics retrieval algorithm to retrieve XCO<sub>2</sub> in the flight test area, the use of regression modeling to estimate the approximate XCO<sub>2</sub> surface, and the use of the HASM platform to model the XCO<sub>2</sub> surface. Section 4 analyzes the retrieval results and distribution of XCO<sub>2</sub> in the flight test area. Section 5 concludes the paper and discusses future work.

## 2. Study Area and Data

### 2.1. Flight Logistics and Data

TanSat aims to deliver XCO<sub>2</sub> in ppm at a high spatial resolution in square grids measuring 3 km on a side. An evaluation of the performance of the TanSat imaging spectrometer prototype was conducted as part of flight tests on the 11th, 14th and 16th of September, 2015. The flight demand parameters, such as the flight height, flight speed, flight time, solar zenith angle, flight geometric requirements and meteorological conditions, can be seen in Table 1.

**Table 1.** Flight parameters.

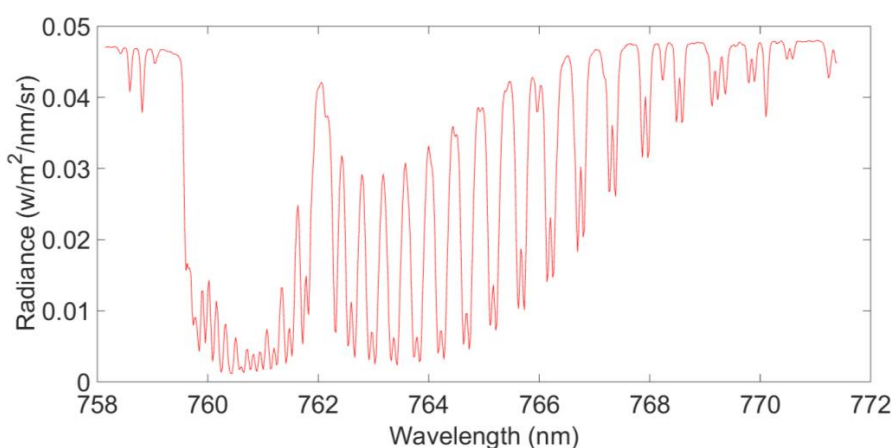
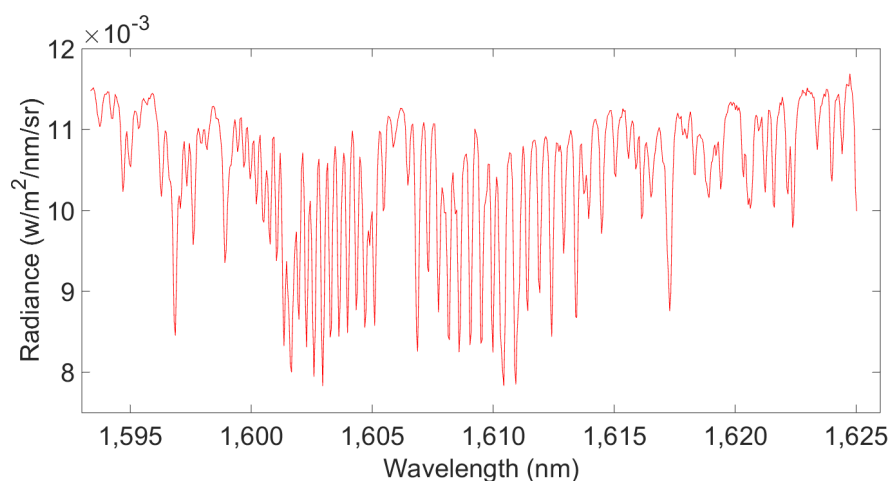
Type	Parameters
Flight height	5 km ± 30 m
Flight speed	220 ± 6.6 km/h
Flight time	10:30–13:30
Solar zenith angle	40°–55°
Flight geometric requirements	Flight drift angle is <5°; range of three-axis attitude angle is <2°; route is straight and course deviation is <60 m.
Meteorological conditions	Good weather with visibility >10 km.

The flight’s spectrometer covered two of the three NIR spectral bands that will be included in the final TanSat spectrometer (Table 2). We can see that band 1 observed the O<sub>2</sub> A-band spectral region (758–773 nm) at 0.044 nm spectral resolution and that Band 2 covers the 1592–1625 nm spectral region with a spectral resolution of 0.13 nm. The third TanSat spectral band (2060 nm), which will provide CO<sub>2</sub> absorption and water vapour information, was not included in the prototype and flight test due to cost.

**Table 2.** NIR spectral bands used for the flight retrieval.

	Band 1	Band 2
Wavelength range (nm)	758–772	1592–1625
Spectral resolution (nm)	0.044	0.13

For this study, we acquired the flight test’s L1B data (calibrated and geographically located spectral radiances) from the Changchun Institute of Optics, Fine Mechanics and Physics, Chinese Academy of Sciences. They had processed the dark background and calibrated the spectral radiation for the test flight’s L1A DN (digital number) data. Samples of two NIR spectral bands derived from the L1B data used in the study can be seen in Figures 1 and 2. The X-axis shows spectral wavelengths (in nm), and the Y-axis represents the spectral radiance (in  $W/m^2/nm/sr$ ). Band 1 contains  $O_2$  absorption information and can be used to estimate the  $O_2$  column with high near-surface sensitivity. Similarly, band 2 contains  $CO_2$  weak absorption information and can be used to estimate the  $CO_2$  column with high near-surface sensitivity.

**Figure 1.** Band 1’s flight test observational L1B data: spectral radiance in 760 nm.**Figure 2.** Band 2’s flight test observational L1B data: spectral radiance in 1610 nm.

## 2.2. Study Area and Surface Characteristics

The flight test passed over Xianghai Reserve and Chagan Lake in Jilin Province (Figure 3). The underlying surface included several lakes, forest, grass, and wetlands, farmland, a thermal power

plant and numerous cities and villages. The test area runs from 122.205° E to 124.946° E and from 44.980° N to 45.360° N and cover an area of about 11,000 km<sup>2</sup>. The left red box of Figure 3 covers the Xianghai Reserve and includes the Limin grassland, Hedao wetland and Xianghai Lake. The right red box of Figure 3 shows the Chagan Lake area and includes the Chanshan town thermal power plant, farmland, Chagan Lake and Songyuan City.

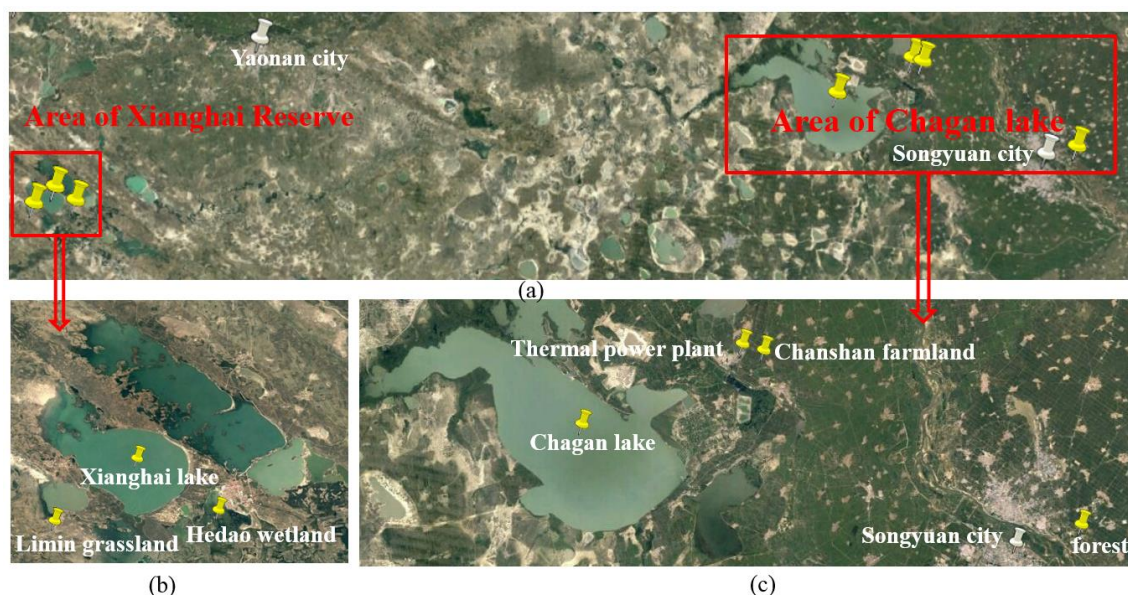


**Figure 3.** The flight test area showing: (a) the overall flight test area; (b) Xianghai Reserve; and (c) the Chagan Lake area.

Ground synchronous observations were also collected during the flight period, and provided important auxiliary data for XCO<sub>2</sub> retrieval and simulation in the flight test area. The observations and methods used to gather them are listed in Table 3. Temperature, humidity, pressure and wind profiles were obtained by sonde measurements and used to summarize the state of the atmosphere for XCO<sub>2</sub> retrieval and surface estimation (Table 3). The CO<sub>2</sub> concentration at the surface was observed with a Greenhouse gas online laser analyzer. The CO<sub>2</sub> profile gathered with a captive balloon and CO<sub>2</sub> concentration in the surface layer were used as dependent variables in the flight test area when we established the approximate XCO<sub>2</sub> surface. Aerosol optical depth and surface reflectance are also crucial factors for XCO<sub>2</sub> retrieval and were observed with a sun photometer and ASD spectrometer, respectively.

**Table 3.** List of ground observations and methods used to gather them.

Observations	Observation Methods Used
Temperature profile	Sonde measurement
Humidity profile	Sonde measurement
Pressure profile	Sonde measurement
Wind profile	Sonde measurement
CO <sub>2</sub> profile	Captive balloon
CO <sub>2</sub> concentration in surface layer	Greenhouse gases online laser analyzer UGGA
Surface reflectance	Analytical Spectral Devices (ASD) spectrometer
Aerosol optical depth	Sun photometer CE318

### 3. Methods

We first retrieved the XCO<sub>2</sub> using a full physics retrieval algorithm. However, it is difficult to directly analyze the spatial distribution of XCO<sub>2</sub> in the flight test area using the limited retrieval results. The high accuracy surface modeling (HASM) method has been widely used in the simulation of climate change, CO<sub>2</sub> concentrations in the surface layer, and terrestrial land cover change [17–19]. We therefore used HASM to fill the gaps where there was no information on XCO<sub>2</sub> in the flight test area. The entire workflow reproduced in Figure 4 includes three main steps. First, we used a full physics retrieval algorithm to retrieve XCO<sub>2</sub>. Second, we used regression modeling to establish the approximate (i.e., not very accurate) surface of XCO<sub>2</sub> in the flight test area. And third, we used HASM, which took the approximate surface of XCO<sub>2</sub> as its driving field and retrieved XCO<sub>2</sub> as its optimum control constraints, to simulate a high accuracy XCO<sub>2</sub> surface for the whole flight test area.

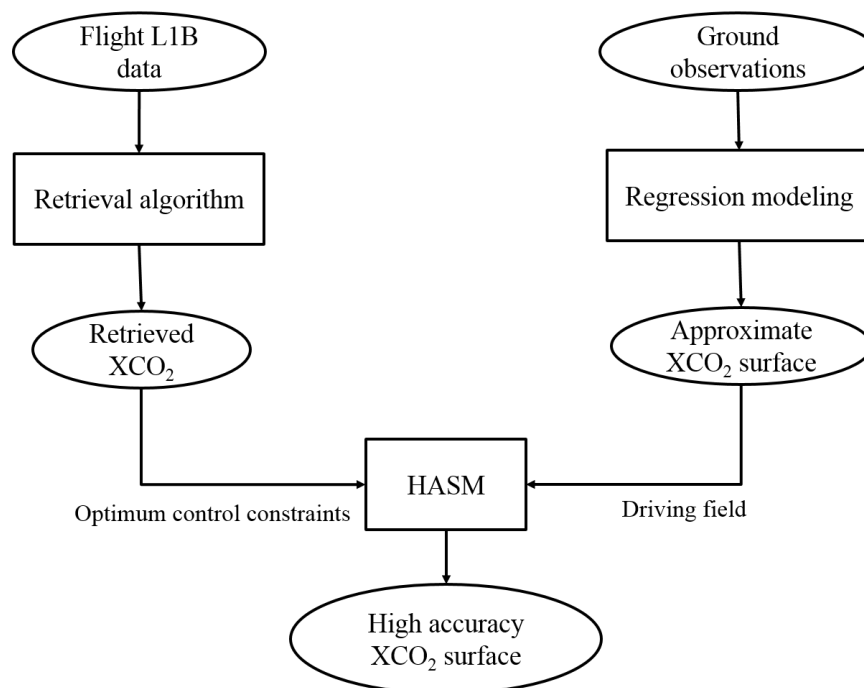


**Figure 4.** The overall workflow.

#### 3.1. Retrieval Algorithm

In this study, the retrieval algorithm is primarily used for simultaneously fitting the O<sub>2</sub> A-band at 760 nm and the CO<sub>2</sub> band at 1610 nm to get column abundances of CO<sub>2</sub> and O<sub>2</sub> based on the optimal estimation method [20]. The retrieval algorithm is an iterative retrieval method which calls the radiative transfer model with updated parameters after each iteration step. The primary components of the flight XCO<sub>2</sub> retrieval processing workflow are summarized in Figure 5. Given that the atmospheric and surface states and the observing geometry for a sounding, the forward model generates radiance spectra and Jacobians (as will be described in more detail in Section 3.1.1 below). This model first generates two synthetic spectra that fully resolves the solar spectrum, the absorption and scattering cross sections for each atmospheric gas and the reflecting surface. The inverse method is based on Rodgers's optimal estimation approach. This method modifies the initial state vector to minimize differences between the observed and simulated spectra from each sounding. This inverse method is described in more detail in Section 3.1.2 below.

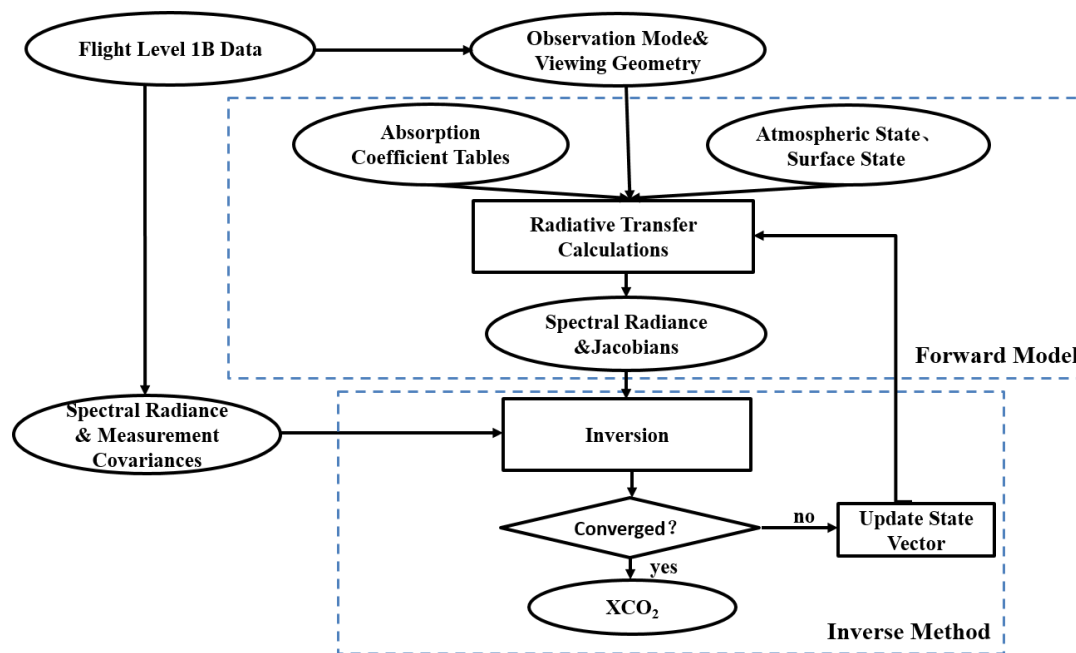


Figure 5. Major components and tasks included in the retrieval algorithm workflow.

### 3.1.1. Forward Model

Synthetic spectra were generated using a radiative transfer algorithm. Losses can be caused by absorption and the scattering of the atmosphere. The sources (i.e., gains) mainly come from atmospheric emission and multiple scattering, and the general expression of the radiative transfer is given by the following equation [21]:

$$\mu \frac{dI(\tau, \mu)}{d\tau} = I(\tau, \mu) - J(\tau, \mu) \quad (1)$$

where  $\mu$  is the cosine of the zenith angle,  $I$  is the specific intensity,  $J$  is the source function (multiple scattering), and  $\tau$  is the optical depth.

The radiative transfer model SCIATRAN was used to solve Equation (1). SCIATRAN is a comprehensive software package for the modeling of radiative transfer processes in the terrestrial atmosphere and ocean in the spectral range from the ultraviolet to the thermal infrared (i.e., 0.18–40  $\mu\text{m}$ ) including multiple scattering processes, polarization, thermal emission and ocean-atmosphere coupling. The software is capable of modeling spectral and angular distributions of the intensity or the Stokes vector of the transmitted, scattered, reflected, and emitted radiation assuming either a plane-parallel or a spherical atmosphere [22].

The inputs and outputs of the SCIATRAN model can be seen in the Table 4. The solar irradiance spectra were acquired from Dr. Kurucz (<http://kurucz.harvard.edu>). Gas absorption and scattering cross sections were obtained from the SCIATRAN software package which incorporates a climatological database obtained from a 2D chemical transport model. The atmospheric state (temperature, humidity and pressure profiles), surface state and aerosol optical properties were taken from ground synchronous observations and the European Centre for Medium-Range Weather Forecasts (ECMWF) reanalysis data. A set of instrument line shape functions were provided by the Changchun Institute of Optics, Fine Mechanics and Physics, Chinese Academy of Sciences. The outputs of the forward model were synthetic spectra and Jacobians.

**Table 4.** SCIATRAN model inputs and outputs.

Inputs	Outputs
Solar irradiance spectra	Radiance spectrum
Gas absorption and scattering cross sections	Jacobians (partial derivatives of the radiance spectrum with respect to each of the state vector elements)
Atmospheric state	-
Surface state	-
Instrument line shape function	-
Aerosol optical properties	-

### 3.1.2. Inverse Method

The inversion was used to obtain the unknown geophysical parameters (CO<sub>2</sub> and O<sub>2</sub> profiles) which minimize the differences between the observed and synthetic spectra from each sounding. The inverse method is based on Rodger's optimization algorithm in which the spectrum is expressed symbolically as in Equation (2):

$$y = F(x, b) + \epsilon \quad (2)$$

where  $x$  is the unknown state vector,  $b$  is a set of quantities required by the forward model but not retrieved,  $F$  is the forward model, and  $\epsilon$  are the spectral errors due to the measurements and the forward model.

To find the state vector with the maximum a posteriori probability, we minimized the cost function (Equation (3)):

$$\chi^2 = (y - F(x, b))^T S_{\epsilon}^{-1} (y - F(x, b)) + (x - x_a)^T S_a^{-1} (x - x_a) \quad (3)$$

where  $S_{\epsilon}$  is the error covariance matrix corresponding to the measurement vector,  $x_a$  is the a priori state vector which holds the prior knowledge about the state vector elements and  $S_a$  is the corresponding a priori error covariance matrix which specifies the uncertainties of the a priori state vector elements as well as their cross-correlations.

The Levenberg-Marquardt method was used to obtain the solution in an iterative manner (Equation (4)):

$$x_{i+1} = x_i + \tilde{S} [K_i^T S_{\epsilon}^{-1} (y - F(x_i, b)) - S_a^{-1} (x_i - x_a)] \quad (4)$$

$$\tilde{S} = \left( K_i^T S_{\epsilon}^{-1} K_i + (1 + \gamma) S_a^{-1} \right)^{-1} \quad (5)$$

where  $K$  is the Jacobian or weighting function matrix consisting of the derivatives of the forward model with respect to the state vector elements  $K = \partial F(x, b) / \partial x$ . In the case of convergence,  $x_{i+1}$  is the most probable solution given the measurements and prior knowledge and it is then denoted as the maximum a posteriori solution  $\tilde{x}$  of the inverse problem.  $\tilde{S}$  is the corresponding covariance matrix consisting of the variances of the retrieval state vector elements and their correlations. The damping factor  $\gamma$  adjusts the step size of the iteration in a way which ensures that each step further minimizes the cost function.

The inverse method continued to provide iterative improvements of the solutions until both of convergence criteria listed below were achieved and we could obtain CO<sub>2</sub> and O<sub>2</sub> column abundances:

- (1) The fitted residuals with root mean square error (RMSE) differences between synthetic and observation spectra less than some pre-determined threshold: 0.25% for CO<sub>2</sub> and 2% for O<sub>2</sub> window [4,13].
- (2) The normalized successive difference of the state vector is less than some pre-determined threshold (1%) in the TANSO-FTS SWIR L2 algorithm (see [2] for details).

For CO<sub>2</sub> we derived column-averaged dry air mole fractions by normalizing the CO<sub>2</sub> columns with the simultaneously retrieved oxygen columns retrieved from the O<sub>2</sub> A-band. Oxygen is an

accurate proxy for the air column because its mole fraction is well known and has negligibly small variations. Then  $XCO_2$  was calculated using Equation (6) [4,23] as follows:

$$XCO_2 = \frac{CO_2^{col}}{o_2^{col}/o_2^{mf}} \quad (6)$$

where  $CO_2^{col}$  is the retrieved absolute  $CO_2$  column (in molecules/cm<sup>2</sup>),  $o_2^{col}$  is the retrieved absolute  $O_2$  column (in molecules/cm<sup>2</sup>), and  $o_2^{mf}$  (0.2095) is the assumed (column-averaged) mole fraction of  $O_2$  used to convert the  $O_2$  column into a corresponding dry air column.

### 3.2. Derivation of Approximate $XCO_2$ Surface

The approximate  $XCO_2$  surface in the flight test area was required to establish as the driving field of HASM (described in Section 3.3 below). The processing steps used to estimate the approximate  $XCO_2$  are summarized in Figure 6. Firstly, we used the least squares fit for the captive balloon's  $CO_2$  profiles, the surface  $CO_2$  concentration in the surface layer and other synchronous ground observations to build a regression model [17,18]. Secondly, we combined the regression model with the Weather Research and Forecasting (WRF) model [24,25] to derive the approximate  $CO_2$  surface for every pressure layer in the whole flight test area. Finally, the pressure weighting function was used to merge every pressure layer's  $CO_2$  surface to estimate the approximate  $XCO_2$  surface.

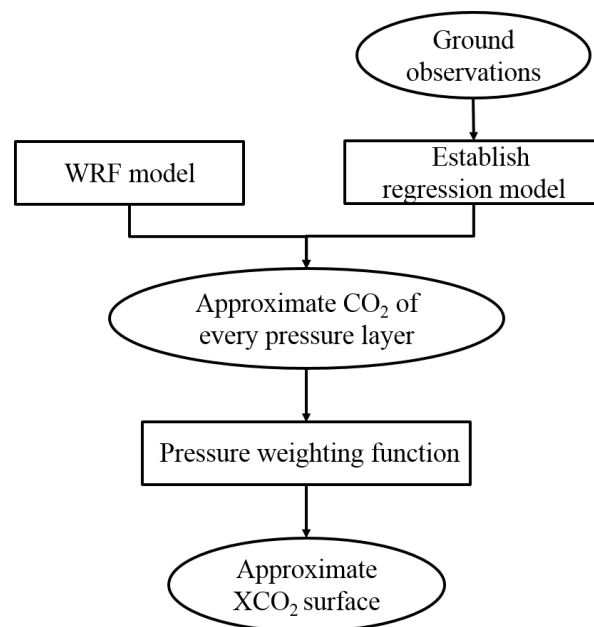


**Figure 6.** Workflow used to estimate approximate  $XCO_2$  surface.

#### 3.2.1. Initial Regression Model

We used an ordinary least squares multivariate linear fit method to build the regression models. The two groups of explanatory variables listed in Table 5 were used to build separate regression models for the  $CO_2$  concentrations in the surface layer [18] and the  $CO_2$  profile. We used the modeling spatial relationships/ordinary least square tools in ArcGIS to perform this work, and both models passed the F test at the 95% confidence level.

**Table 5.** Explanatory variables used to model CO<sub>2</sub> in different layers.

Dependent Variables	Explanatory Variables
CO <sub>2</sub> concentration in surface layer	Surface pressure, atmospheric humidity, atmospheric temperature, soil humidity, soil temperature, upward and downward shortwave radiation, altitude, longitude and latitude
CO <sub>2</sub> profile (not including surface layer)	Temperature, pressure and humidity profiles, wind speed and direction, latitude and longitude

The CO<sub>2</sub> concentration in every pressure layer at every grid point in the flight test area was then calculated as follows:

$$Y_{CO_2} = b + \sum_{i=1}^n a_i x_i \quad (7)$$

where  $Y_{CO_2}$  is the CO<sub>2</sub> concentration in every pressure layer,  $b$  is a constant,  $x$  represents the explanatory variables,  $a$  is the corresponding coefficient for each of the explanatory variables, and  $n$  is the number of explanatory variables.

### 3.2.2. WRF Model

WRF is a next-generation mesoscale numerical weather prediction system designed for both atmospheric research and operational forecasting needs. The model serves a wide range of meteorological applications across scales from tens of meters to thousands of kilometers. WRF can generate atmospheric simulations using real-world data or idealized conditions. WRF offers operational forecasting a flexible and computationally-efficient platform for operational forecasting using initial data from the US National Center for Environmental Prediction (NCEP).

The initial data used in this study were derived from reanalysis datasets of NCEP. We generated forecasts at 20:00 each day using an integrate interval of 30 h and 1 km by 1 km grid. Physical parameters were the YSU scheme, Monin Obukhov scheme, WSM 6-class graupel scheme, RRTM scheme (longwave), Goddard scheme (shortwave), Noah-MP land-surface model and Kain-Fritsch (new Eta) scheme respectively. We used WRF Version 3.5 to model the CO<sub>2</sub> concentration at every point using the aforementioned explanatory variables in the flight test area on an hourly basis from 10:00 to 14:00 on the 11th, 14th, and 16th of September. We then used Equation (7) to calculate the approximate CO<sub>2</sub> concentration of every pressure layer at each point in the flight test area.

### 3.2.3. Pressure Weighting Function

The pressure weighting function  $h$  relates the local CO<sub>2</sub> concentration specified on the discrete pressure levels to the profile-weighted average [8], so  $X_{CO_2}$  could be calculated as follows:

$$X_{CO_2} = \sum_{i=1}^n h_i u_i \quad (8)$$

where  $u$  denotes the CO<sub>2</sub> concentration and the subscripts refer to the layers, and:

$$h_i = \left| \left( -p_i + \frac{p_{i+1} - p_i}{\ln(p_{i+1}/p_i)} \right) + \left( p_i - \frac{p_i - p_{i-1}}{\ln(p_i/p_{i-1})} \right) \right| \frac{1}{p_{surf}} \quad (9)$$

where  $p$  denotes the pressure and the subscripts again refer to the layers, and  $p_{surf}$  denotes the surface pressure. For the edge layers, if  $i = 1$ , only the left first term applies, that is  $h_1 = \left| \left( -p_1 + \frac{p_2 - p_1}{\ln(p_2/p_1)} \right) \right| \frac{1}{p_{surf}}$ , while if  $i = n$ , only the left second term applies, that is  $h_n = \left| \left( p_n - \frac{p_n - p_{n-1}}{\ln(p_n/p_{n-1})} \right) \right| \frac{1}{p_{surf}}$ .

The approximate CO<sub>2</sub> concentration for every pressure layer at each point in the flight test area was calculated using the methods described in Sections 3.2.1 and 3.2.2. With the methods specified at

this step, the approximate  $XCO_2$  was obtained by averaging the approximate  $CO_2$  concentration of every pressure layer, weighted by the pressure weighting function.

### 3.3. High Accuracy Surface Modeling

The high accuracy surface modeling [26] platform takes global approximate information (e.g., remote sensing images or model simulation results) as its driving field and local accurate information (e.g., ground observation and/or sampling data) as its optimum control constraints. A surface can be uniquely defined by the first and the second fundamental coefficients [27–31] in terms of the fundamental theorem of surfaces. The first fundamental coefficients are used to express the intrinsic geometric properties that do not depend on the shape of the surface, but only on measurements that we can carry out while on the surface itself. The second fundamental coefficients reflect the local warping of the surface, namely its deviation from a tangent plane at the point under consideration, which can be observed from outside the surface. The Earth's surface system or a component surface of the Earth's surface environment can be simulated with HASM when its spatial resolution is fine enough and is uniquely defined by both extrinsic and intrinsic invariants of the surface.

If a surface is a graph of a function  $z = f(x, y)$ , the first fundamental coefficients  $E$ ,  $F$  and  $G$  can be formulated as

$$\begin{cases} E = 1 + f_x^2 \\ G = 1 + f_y^2 \\ F = f_x \cdot f_y \end{cases} \quad (10)$$

The second fundamental coefficients  $L$ ,  $M$  and  $N$  can be formulated as

$$\begin{cases} L = \frac{f_{xx}}{\sqrt{1+f_x^2+f_y^2}} \\ N = \frac{f_{yy}}{\sqrt{1+f_x^2+f_y^2}} \\ M = \frac{f_{xy}}{\sqrt{1+f_x^2+f_y^2}} \end{cases} \quad (11)$$

The first and the second fundamental coefficients should satisfy the following Gauss equation set:

$$\begin{cases} f_{xx} = \Gamma_{11}^1 \cdot f_x + \Gamma_{11}^2 \cdot f_y + L \cdot (E \cdot G - F^2)^{-1/2} \\ f_{yy} = \Gamma_{22}^1 \cdot f_x + \Gamma_{22}^2 \cdot f_y + N \cdot (E \cdot G - F^2)^{-1/2} \\ f_{xy} = \Gamma_{12}^1 \cdot f_x + \Gamma_{12}^2 \cdot f_y + M \cdot (E \cdot G - F^2)^{-1/2} \end{cases} \quad (12)$$

where  $\Gamma_{11}^1 = \frac{1}{2} (G \cdot E_x - 2F \cdot F_x + F \cdot E_y) \cdot (E \cdot G - F^2)^{-1}$ ,  $\Gamma_{12}^1 = \frac{1}{2} (G \cdot E_y - F \cdot G_x) \cdot (E \cdot G - F^2)^{-1}$ ,  $\Gamma_{22}^1 = \frac{1}{2} (2G \cdot F_y - G \cdot G_x - F \cdot G_y) \cdot (E \cdot G - F^2)^{-1}$ ,  $\Gamma_{11}^2 = \frac{1}{2} (2E \cdot F_x - E \cdot E_y - F \cdot E_x) \cdot (E \cdot G - F^2)^{-1}$ ,  $\Gamma_{12}^2 = \frac{1}{2} (E \cdot G_x - F \cdot E_y) \cdot (E \cdot G - F^2)^{-1}$ ,  $\Gamma_{22}^2 = \frac{1}{2} (E \cdot G_y - 2F \cdot F_y + F \cdot G_x) \cdot (E \cdot G - F^2)^{-1}$  are the Christoffel symbols of the second kind which depend only on the first fundamental coefficients and their derivatives.

Finite difference methods are used for solving the Gauss equation set (Equation (12)). It can be simplified as the following equation set [26]:

$$\begin{cases} A \cdot z^{(n+1)} = d^{(n)} \\ B \cdot z^{(n+1)} = q^{(n)} \\ C \cdot z^{(n+1)} = p^{(n)} \end{cases} \quad (13)$$

If  $f_{i,j}$  is the value of  $z = f(x, y)$  at the  $p$ th sampled point  $(x_i, y_i)$  in the computational domain, the simulation value should be equal or approximate to the sampling value of this lattice so that the

constraint equation is added to the simplified equation set (Equation (13)). The matrix formulation of the HASM master equations can be expressed as follows [26]:

$$\begin{bmatrix} A^T & B^T & C^T & \lambda \cdot S^T \end{bmatrix} \begin{bmatrix} A \\ B \\ C \\ \lambda \cdot S \end{bmatrix} z^{(n+1)} = \begin{bmatrix} A^T & B^T & C^T & \lambda \cdot S^T \end{bmatrix} \begin{bmatrix} d^{(n)} \\ q^{(n)} \\ p^{(n)} \\ \lambda \cdot k \end{bmatrix} \quad (14)$$

where the parameter  $\lambda$  is the weight of the sampling points and determines the contribution of the sampling points to the simulated surface.  $\lambda$  could be a real number, which means all sampling points have the same weight, or a vector, which means every sampling point has its own weight. An area affected by a sampling point in a complex region is smaller than in a flat region. Therefore, a smaller value of  $\lambda$  is selected in a complex region and a bigger value of  $\lambda$  is selected in a flat region.

High accuracy surface modeling can simulate continuous attribute variations in three-dimensional space, and has been successfully used in simulating climate change [17,32,33], constructing DEMs [28,29], interpolating soil properties [34–36] and terrestrial land cover change [19]. For this study, HASM took the approximate XCO<sub>2</sub> surface as its driving field and the flight retrieved XCO<sub>2</sub> as its optimum control constraints as shown in Equation (15):

$$X_{\text{sim}} = \text{HASM}(X_{\text{initial}}, X_{\text{sam}}) \quad (15)$$

where  $X_{\text{sim}}$  is the final XCO<sub>2</sub> surface which is calculated by HASM,  $X_{\text{initial}}$  is the approximate XCO<sub>2</sub> surface which is obtained by regression modeling, and  $X_{\text{sam}}$  is the retrieval XCO<sub>2</sub>. The main inputs of HASM are the retrieval XCO<sub>2</sub> and the approximate XCO<sub>2</sub> surface with the output being the high accuracy surface of XCO<sub>2</sub>.

## 4. Results

### 4.1. Retrieval XCO<sub>2</sub>

The XCO<sub>2</sub> concentrations estimated with the full physics retrieval approach for about 400 points in the flight test area covering seven kinds of underlying surface—grassland, water, wetland, farmland, a thermal power plant, urban area and forest land—are shown in Figure 7.

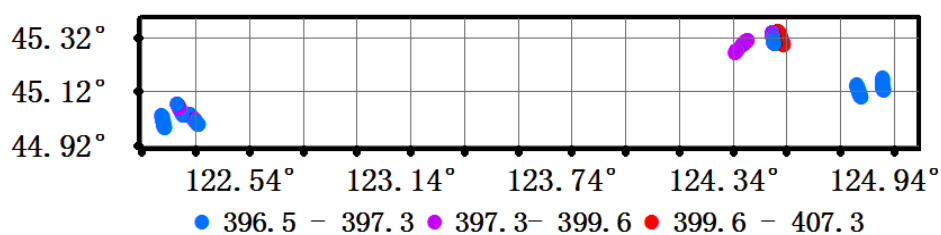


**Figure 7.** XCO<sub>2</sub> concentrations estimated in the flight test area using full physics retrieval approach.

The retrieval XCO<sub>2</sub> concentrations ranged from 396.5 to 407.3 ppm with a mode of 396.5 to 397.3 ppm (Figure 7).

### 4.2. Approximate XCO<sub>2</sub> Surface in the Flight Test Area

In order to model the high accuracy XCO<sub>2</sub> surface, we first established the approximate XCO<sub>2</sub> surface using an ordinary linear least squares regression model to represent the spatial relationships in the flight test area (Figure 8).

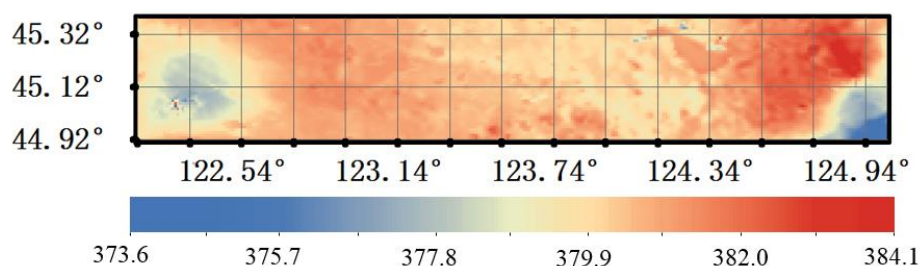


**Figure 8.** Approximate XCO<sub>2</sub> surface in the flight test area.

From Figures 3 and 8, we can see that the mean XCO<sub>2</sub> of this approximate surface is about 20 ppm lower than the retrieval XCO<sub>2</sub> surface, but does show the estimated spatial relationships in the flight test area. It was used as the driving field of HASM, and the retrieval XCO<sub>2</sub> was used as the optimum control constraints to model the XCO<sub>2</sub> surface in the flight test area.

#### 4.3. High Accuracy XCO<sub>2</sub> Surface

The high accuracy surface model took the regression results as its driving field and the retrieval XCO<sub>2</sub> values as its optimum control constraints to more accurately estimate the XCO<sub>2</sub> surface in the whole flight test area (Figure 9).

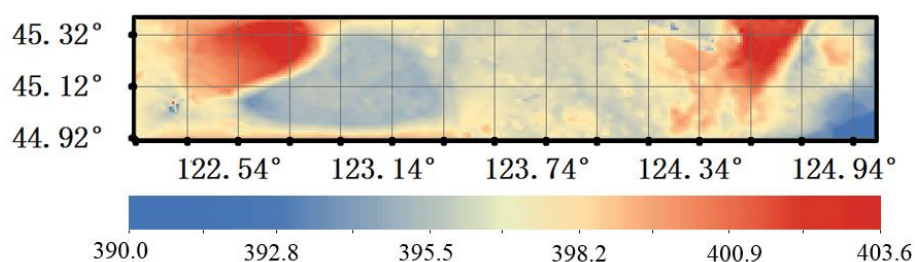


**Figure 9.** The XCO<sub>2</sub> concentrations in the flight test area estimated with HASM.

The HASM XCO<sub>2</sub> estimates in the flight test area ranged from 390.0 to 403.6 ppm. Combining the map in Figure 9 with the image showing the flight test area (Figure 3), we can see that XCO<sub>2</sub> is highest in Songyuan City. Similarly, the XCO<sub>2</sub> in another small city, Taonan, is higher as well. The XCO<sub>2</sub> was lower in the Xianghai Reserve, which includes the Limin grassland, Hedao wetland and Xianghai Lake. The aforementioned results show how human activities can increase XCO<sub>2</sub> and that the retrieval XCO<sub>2</sub> calculated in this study was sensitive to the boundary layer which may be affected by human's activities over relatively short distances.

#### 4.4. Comparison with OCO-2's XCO<sub>2</sub> Estimates

The Orbiting Carbon Observatory 2 (OCO-2) which was launched on 2 July 2014, is NASA's first dedicated Earth remote sensing satellite to study XCO<sub>2</sub> from Space. OCO-2 is collecting space-based global measurements of XCO<sub>2</sub> with the precision, resolution, and coverage needed to characterize sources and sinks on regional scales. OCO-2 is also able to quantify CO<sub>2</sub> variability over seasonal cycles year after year. The OCO-2 instrument flies on a dedicated spacecraft and includes three high-resolution grating spectrometers which make coincident measurements of reflected sunlight in the near-infrared CO<sub>2</sub> near 1610 and 2060 nm and in the molecular oxygen (O<sub>2</sub>) A-Band at 760 nm at a resolution of 1.29 (longitude) and 2.25 km (latitude). The XCO<sub>2</sub> (Version OCO2\_L2\_Lite\_FP.7r) at the 14 locations in the flight test area ranged from 396.7 to 398.3 ppm on 11–16 September 2014 (Figure 10).

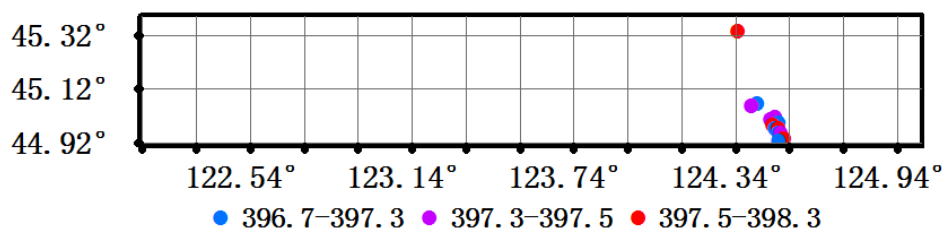


Figure 10. The XCO<sub>2</sub> estimates from OCO-2 in the flight test area.

The corresponding HASM XCO<sub>2</sub> estimates were extracted from Figure 9 and used to calculate the differences from the OCO-2 XCO<sub>2</sub> estimates (Table 6).

Table 6. The XCO<sub>2</sub> difference between HASM and OCO-2 estimates in the flight test area.

Number	Longitude (°)	Latitude (°)	Flight Test (ppm)	OCO-2 (ppm)	Difference (ppm)
1	124.35	45.34	396.67	398.34	−1.67
2	124.40	45.06	399.13	397.54	1.59
3	124.42	45.07	398.85	397.07	1.78
4	124.47	45.01	398.05	397.35	0.70
5	124.48	45.00	398.36	397.49	0.87
6	124.48	44.99	398.05	397.84	0.21
7	124.49	45.02	398.75	397.42	1.33
8	124.49	44.98	397.82	397.25	0.57
9	124.50	45.00	399.01	397.23	1.78
10	124.50	44.98	398.73	397.63	1.10
11	124.50	44.96	397.99	396.73	1.26
12	124.50	44.93	397.24	397.04	0.20
13	124.51	44.96	397.92	397.29	0.63
14	124.52	44.94	397.35	397.87	−0.52

Twelve of the 14 HASM XCO<sub>2</sub> estimates were higher than the corresponding OCO-2 estimates (column 6, Table 6) with the mean difference and standard deviation being 0.7 and 0.95 ppm, respectively. Given that the accuracy of the OCO-2 XCO<sub>2</sub> estimates is about 1 ppm [37], the HASM modeling results based on the flight test of the TanSat instruments fell within the expected range.

## 5. Conclusions

This paper presents the validation of XCO<sub>2</sub> based on a flight test of TanSat instruments using a combination of full physics and surface modelling. The results produced with this pair of methods were nevertheless sufficiently similar to justify using HASM to estimate the XCO<sub>2</sub> surface. HASM took the approximate surface of XCO<sub>2</sub> as its driving field and the flight's retrieval XCO<sub>2</sub> as its optimum control constraints to fill in the gaps across the whole flight test area. The results showed that the XCO<sub>2</sub> in cities is higher than in other places suggesting that cities are places where human activities can lead to increased XCO<sub>2</sub> concentrations. Compared with OCO-2's XCO<sub>2</sub>, the mean difference is 0.7 ppm and the standard deviation is 0.95 ppm. Due to the good matching, the surface modelling of XCO<sub>2</sub> based on the flight test of TanSat instruments fell within an expected and accepted range.

The flight test in this study was conducted in good weather conditions, so we assumed the sky was clear when the retrieval XCO<sub>2</sub> estimates were acquired. In fact, the presence of clouds and aerosols could influence XCO<sub>2</sub> and in the future, we plan to consider their impact. Moreover, the CO<sub>2</sub> strong absorption band (i.e., 2060 nm) contains additional information on CO<sub>2</sub> and H<sub>2</sub>O, but we did not use this band for the current flight test due to cost. Therefore, we will conduct XCO<sub>2</sub> retrieval using three bands from other satellite data before TanSat is launched in the future.

**Acknowledgments:** This work was supported by the National Natural Science Foundation of China (Grant No. 91325204), the National High-tech R&D Program of the Ministry of Science and Technology of China (Grant No. 2013AA122003), and the National Key Technologies R&D Program of the Ministry of Science and Technology of China (Grant No. 2013BACO3B05). We are grateful to the OCO-2 teams for sharing the OCO-2 observations used in this paper.

**Author Contributions:** Li Li Zhang and Tian Xiang Yue conceived and designed the experiments; Li Li Zhang performed the experiments; Chao Lin and Yu Quan Zheng supplied the data; Yu Liu and Jian Hong Guo participated in the data processing; Na Zhao, Zheng Ping Du and Yi Fu Wang contributed analysis tools; Li Li Zhang wrote the paper; John Peter Wilson, Ding Yi Wang and Dong Dong Liu supervised the revision of the manuscript.

**Conflicts of Interest:** The authors declare no conflict of interest.

## References

1. Meehl, G.A.; Washington, W.M. El Nino-like climate change in a model with increased atmospheric CO<sub>2</sub> concentrations. *Nature* **1996**, *382*, 56–60. [[CrossRef](#)]
2. Yoshida, Y.; Ota, Y.; Eguchi, N.; Kikuchi, N.; Nobuta, K.; Tran, H.; Morino, I.; Yokota, T. Retrieval algorithm for CO<sub>2</sub> and CH<sub>4</sub> column abundances from short-wavelength infrared spectral observations by the Greenhouse gases observing satellite. *Atmos. Meas. Tech.* **2011**, *4*, 717–734. [[CrossRef](#)]
3. Oshchepkov, S.; Bril, A.; Maksyutov, S.; Yokota, T. Detection of optical path in spectroscopic space-based observations of greenhouse gases: Application to GOSAT data processing. *J. Geophys. Res.* **2011**, *116*, D14304. [[CrossRef](#)]
4. Schneising, O.; Buchwitz, M.; Burrows, J.P.; Bovensmann, H.; Reuter, M.; Notholt, J.; Macatangay, R.; Warneke, T. Three years of greenhouse gas column-averaged dry air mole fractions retrieved from satellite—Part 1: Carbon dioxide. *Atmos. Meas. Tech.* **2008**, *8*, 3827–3853. [[CrossRef](#)]
5. Guerlet, S.; Butz, A.; Schepers, D.; Basu, S.; Hasekamp, O.P.; Kuze, A.; Yokota, T.; Blavier, J.F.; Deutscher, N.M.; Griffith, D.W.T.; et al. Impact of aerosol and thin cirrus on retrieving and validating XCO<sub>2</sub> from GOSAT shortwave infrared measurements. *J. Geophys. Res.* **2013**, *118*, 4887–4905.
6. Boesch, H.; Toon, G.C.; Sen, B.; Washenfelder, R.A.; Wennberg, P.O.; Buchwitz, M.; Beek, R.D.; Burrows, J.P.; Crisp, D.; Christi, M.; et al. Space-Based near-infrared CO<sub>2</sub> measurements: Testing the Orbiting Carbon Observatory retrieval algorithm and validation concept using SCIAMACHY observations over Park Falls, Wisconsin. *J. Geophys. Res.* **2006**, *111*, D23302.
7. Boesch, H.; Baker, D.; Connor, B.; Crisp, D.; Miller, C. Characterization of CO<sub>2</sub> Column Retrievals from Shortwave-Infrared Satellite Observations of the Orbiting Carbon Observatory-2 Mission. *Remote Sens.* **2011**, *3*, 270–304. [[CrossRef](#)]
8. Connor, B.J.; Boesch, H.; Toon, G.; Sen, B.; Miller, C.; Crisp, D. Orbiting Carbon Observatory: Inverse method and prospective error analysis. *J. Geophys. Res. Atmos.* **2008**, *113*, D05305. [[CrossRef](#)]
9. O'Dell, C.W.; Connor, B.; Boesch, H.; O'Brien, D.; Frankenberg, C.; Castano, R.; Christi, M.; Eldering, D.; Fisher, B.; Gunson, M.; et al. The ACOS CO<sub>2</sub> retrieval algorithm—Part 1: Description and validation against synthetic observations. *Atmos. Meas. Tech.* **2012**, *5*, 99–121. [[CrossRef](#)]
10. Bovensmann, H.; Buchwitz, M.; Burrows, J.P.; Reuter, M.; Krings, T.; Gerilowski, K.; Schneising, O.; Heymann, J.; Tretner, A.; Erzinger, J. A remote sensing technique for global monitoring of power plant CO<sub>2</sub> emissions from space and related applications. *Atmos. Meas. Tech.* **2010**, *3*, 781–811. [[CrossRef](#)]
11. Reuter, M.; Buchwitz, M.; Schneising, O.; Heymann, J.; Bovensmann, H.; Burrows, J.P. A method for improved SCIAMACHY CO<sub>2</sub> retrieval in the presence of optically thin clouds. *Atmos. Meas. Tech.* **2009**, *2*, 2483–2538. [[CrossRef](#)]
12. Schneising, O.; Bergamaschi, P.; Bovensmann, H.; Buchwitz, M.; Burrows, J.P.; Deutscher, N.M.; Griffith, D.W.T.; Heymann, J.; Macatangay, R.; Messerschmidt, J.; et al. Atmospheric greenhouse gases retrieved from SCIAMACHY: Comparison to ground-based FTS measurements and model results. *Atmos. Meas. Tech.* **2012**, *12*, 1527–1540. [[CrossRef](#)]
13. Reuter, M.; Bovensmann, H.; Buchwitz, M.; Burrows, J.P.; Connor, B.J.; Deutscher, N.M.; Griffith, D.W.T.; Heymann, J.; Aleks, G.K.; Messerschmidt, J.; et al. Retrieval of atmospheric CO<sub>2</sub> with enhanced accuracy and precision from SCIAMACHY: Validation with FTS measurements and comparison with model results. *J. Geophys. Res.* **2011**, *116*, D04301. [[CrossRef](#)]

14. Heymann, J.; Reuter, M.; Hilker, M.; Buchwitz, M.; Schneising, O.; Bovensmann, H.; Burrows, J.P.; Kuze, A.; Suto, H.; Deutscher, N.M.; et al. Consistent satellite XCO<sub>2</sub> retrievals from SCIAMACHY and GOSAT using the BESD algorithm. *Atmos. Meas. Tech.* **2015**, *8*, 2961–2980. [[CrossRef](#)]
15. Cogan, J.; Boesch, H.; Parker, R.J.; Feng, L.; Palmer, P.I.; Blavier, J.F.L.; Deutscher, N.M.; Macatangay, R.; Notholt, J.; Roehl, C.; et al. Atmospheric carbon dioxide retrieved from the Greenhouse gases Observing SATellite (GOSAT): Comparison with ground-based TCCON observations and GEOS-Chem model calculations. *J. Geophys. Res.* **2012**, *117*, D21301. [[CrossRef](#)]
16. Crisp, D.; Fisher, B.M.; O'Dell, C.; Frankenberg, C.; Basilio, R.; Boesch, H.; Brown, L.R.; Castano, R.; Connor, B.; Deutscher, N.; et al. The ACOS CO<sub>2</sub> retrieval algorithm—Part II: Global XCO<sub>2</sub> data characterization. *Atmos. Meas. Tech.* **2012**, *5*, 687–707. [[CrossRef](#)]
17. Wang, C.L.; Zhao, N.; Yue, T.X.; Zhao, M.W.; Chen, C. Change trend of monthly precipitation in China with an improved surface modeling method. *Environ. Earth Sci.* **2015**, *74*, 6459–6469. [[CrossRef](#)]
18. Liu, Y.; Guo, J.H.; Yue, T.X.; Zhao, N. Simulation and analysis of carbon dioxide concentration in surface layer. *Geo-Inf. Sci.* **2016**, in press.
19. Yue, T.X.; Fan, Z.M.; Chen, C.F.; Sun, X.F.; Li, B.L. Surface modeling of global terrestrial ecosystems under three climate change scenarios. *Ecol. Model.* **2011**, *222*, 2342–2361. [[CrossRef](#)]
20. Rodgers, C.D. *Inverse Methods for Atmospheric Sounding: Theory and Practice*; World Scientific Publishing: Singapore, 2000.
21. Li, W.B. *Atmospheric Remote Sensing*; Peking University Press: Beijing, China, 2014.
22. Rozanov, V.V.; Rozanov, A.V.; Kokhanovsky, A.A.; Burrows, J.P. Radiative transfer through terrestrial atmosphere and ocean: Software package SCIATRAN. *J. Quant. Spectrosc. Radiat. Transf.* **2014**, *133*, 13–71. [[CrossRef](#)]
23. Wunch, D.; Toon, G.C.; Jean-François, L.B.; Rebecca, A.W.; Notholt, J.; Connor, B.J.; Griffith, D.W.T.; Sherlock, V.; Wennberg, P.O. The Total Carbon Column Observing Network. *Philos. Trans. R. Soc.* **2011**, *369*, 2087–2112. [[CrossRef](#)] [[PubMed](#)]
24. Michalakes, J.; Dudhia, J.; Grill, D.; Klemp, J.; Skamarock, W. Design of a next-generation regional weather research and forecast model. In *Towards Teracomputing: Proceedings of the Eighth ECMWF Workshop on the Use of Parallel Processors in Meteorology*; World Scientific: River Edge, NJ, USA, 1998; pp. 117–124.
25. Michalakes, J.; Chen, S.; Dudhia, J.; Hart, L.; Klemp, J.; Middlecoff, J.; Skamarock, W. Development of a Next Generation Regional Weather Research and Forecast Model. In *Developments in Teracomputing: Proceedings of the Ninth ECMWF Workshop on the Use of High Performance Computing in Meteorology*; World Scientific: Singapore, 2001; pp. 269–276.
26. Yue, T.X. *Surface Modelling: High Accuracy and High Speed Methods*; CRC Press: Boca Raton, FL, USA, 2011.
27. Yue, T.X.; Du, Z.P.; Song, D.J.; Gong, Y. A new method of surface modeling and its application to DEM construction. *Geomorphology* **2007**, *91*, 161–172. [[CrossRef](#)]
28. Yue, T.X.; Chen, C.F.; Li, B.L. An adaptive method of high accuracy surface modeling and its application to simulating elevation surfaces. *Trans. GIS* **2010**, *14*, 615–630. [[CrossRef](#)]
29. Yue, T.X.; Song, D.J.; Du, Z.P.; Wang, W. High-Accuracy surface modelling and its application to DEM generation. *Int. J. Remote Sens.* **2010**, *31*, 2205–2226. [[CrossRef](#)]
30. Yue, T.X.; Wang, S.H. Adjustment computation of HASM: A high-accuracy and high-speed method. *Int. J. Geogr. Inf. Sci.* **2010**, *24*, 1725–1743. [[CrossRef](#)]
31. Yue, T.X.; Zhang, L.L.; Zhao, N.; Zhao, M.W.; Chen, C.F.; Du, Z.P.; Song, D.J.; Fan, Z.M.; Shi, W.J.; Wang, S.H.; et al. A review of recent developments in HASM. *Environ. Earth Sci.* **2015**, *74*, 6541–6549. [[CrossRef](#)]
32. Yue, T.X.; Zhao, N.; Yang, H.; Song, Y.J.; Du, Z.P.; Fan, Z.M.; Song, D.J. The multi-grid method of high accuracy surface modelling and its validation. *Trans. GIS* **2013**, *17*, 943–952. [[CrossRef](#)]
33. Yue, T.X.; Zhao, N.; Ramsey, D.; Wang, C.L.; Fan, Z.M.; Chen, C.F.; Lu, Y.M.; Li, B.L. Climate change trend in China, with improved accuracy. *Clim. Chang.* **2013**, *120*, 137–151. [[CrossRef](#)]
34. Shi, W.J.; Liu, J.Y.; Song, Y.J.; Du, Z.P.; Chen, C.F.; Yue, T.X. Surface modelling of soil pH. *Geoderma* **2009**, *150*, 113–119. [[CrossRef](#)]

35. Shi, W.J.; Liu, J.Y.; Du, Z.P.; Stein, A.; Yue, T.X. Surface modelling of soil properties based on land use information. *Geoderma* **2011**, *162*, 347–357. [[CrossRef](#)]
36. Shi, W.J.; Yue, T.X.; Du, Z.P.; Wang, Z.; Li, X.W. Surface modeling of soil antibiotics. *Sci. Total Environ.* **2016**, *543*, 609–619. [[CrossRef](#)] [[PubMed](#)]
37. Wunch, D.; Wennberg, P.O.; Osterman, G.; Fisher, B.; Naylor, B.; Roehl, C.M.; O'Dell, C.; Mandrake, L.; Viatte, C.; Griffith, D.W.T.; et al. Comparisons of the Orbiting Carbon Observatory-2 (OCO-2) XCO<sub>2</sub> measurements with TCCON. *Atmos. Meas. Tech. Discuss.* **2016**. [[CrossRef](#)]



© 2016 by the authors; licensee MDPI, Basel, Switzerland. This article is an open access article distributed under the terms and conditions of the Creative Commons Attribution (CC-BY) license (<http://creativecommons.org/licenses/by/4.0/>).